Broadening of Cloud Droplet Size Spectra by Stochastic Condensation: Effects of Mean Updraft Velocity and CCN Activation

GAETANO SARDINA

*Department of Meteorology, and Swedish e-Science Research Centre, Stockholm University, Stockholm, and
Division of Fluid Dynamics, Department of Mechanics and Maritime Sciences,
Chalmers University of Technology, Gothenburg, Sweden*

STÉPHANE POULAIN AND LUCA BRANDT

Linné FLOW Centre, and Swedish e-Science Research Centre, KTH Mechanics, Stockholm, Sweden

RODRIGO CABALLERO

Department of Meteorology, and Swedish e-Science Research Centre, Stockholm University, Stockholm, Sweden

(Manuscript received 22 August 2017, in final form 29 October 2017)

ABSTRACT

The authors study the condensational growth of cloud droplets in homogeneous isotropic turbulence by means of a large-eddy simulation (LES) approach. The authors investigate the role of a mean updraft velocity and of the chemical composition of the cloud condensation nuclei (CCN) on droplet growth. The results show that a mean constant updraft velocity superimposed onto a turbulent field reduces the broadening of the droplet size spectra induced by the turbulent fluctuations alone. Extending the authors' previous results regarding stochastic condensation, the authors introduce a new theoretical estimation of the droplet size spectrum broadening that accounts for this updraft velocity effect. A similar reduction of the spectra broadening is observed when the droplets reach their critical size, which depends on the chemical composition of CCN. The analysis of the square of the droplet radius distribution, proportional to the droplet surface, shows that for large particles the distribution is purely Gaussian, while it becomes strongly non-Gaussian for smaller particles, with the left tail characterized by a peak around the haze activation radius. This kind of distribution can significantly affect the later stages of the droplet growth involving turbulent collisions, since the collision probability kernel depends on the droplet size, implying the need for new specific closure models to capture this effect.

1. Introduction

Clouds play a central role in Earth's climate both through their interaction with radiation and through their role in the hydrological cycle. Warm clouds—those in which freezing does not occur—make a large contribution to the planetary albedo especially in the subtropics and produce 30% of the total rainfall globally and 70% of tropical rainfall (Lau and Wu 2003). Both cloud albedo and the rate of rain formation depend crucially on the size distribution of cloud droplets, but fundamental questions remain about the processes controlling the width and shape of this distribution.

When a moist air parcel is adiabatically lifted past its saturation level, water begins to condense around cloud condensation nuclei (CCN). The CCN size (or mass) distribution determines the initial size distribution for the droplets. Further condensational growth of the droplets is inversely proportional to their radius, and this entails an intrinsic tendency for the distribution to become narrower (Pruppacher and Klett 1997). However, observations have long shown that droplet size

---

Corresponding author: Gaetano Sardina, sardina@chalmers.se

distributions in warm clouds are broad and often multimodal (Warner 1969). High-resolution observations show that even the narrowest measured distributions are broader than predicted by a conventional adiabatic parcel model (Brenguier and Chaumat 2001).

There is as yet no complete understanding of the processes that counteract condensational narrowing to broaden the distribution. This uncertainty poses a major roadblock in understanding the formation of warm-cloud precipitation (Devenish et al. 2012; Grabowski and Wang 2013). Growth to raindrop size requires collision and coalescence of droplets, which in turn requires significant velocity differences among droplets. Droplet fall speeds—governed by Stokes's law—increase quadratically with radius, and significant collision rates are only achieved once a substantial subset of droplets has reached a size $O(10)$ μm while those at the lower end of the distribution are still $O(1)$ μm. This "condensation–coalescence bottleneck" in warm clouds remains a major unsolved problem.

Clouds are highly turbulent systems and turbulent stirring, entrainment, and mixing are observed to drive supersaturation and droplet density fluctuations down to centimeter scales (Beals et al. 2015). Turbulence may help overcome the bottleneck by facilitating droplet collisions, both by locally increasing droplet concentration (the inertial clustering effect; Sundaram and Collins 1997) and by generating droplet velocity differences (the sling effect; Falkovich et al. 2002). Here we focus on a different role of turbulence, namely, the broadening of droplet size spectra by differential condensation driven by turbulent supersaturation fluctuations. Droplets caught in the updraft of a turbulent eddy will experience greater supersaturation and will therefore grow faster than those caught in the downdraft (which may even experience subsaturation and evaporative loss). It is plausible that this effect will be stronger for larger eddies with stronger updrafts, so we may expect the resulting broadening to increase with increasing Reynolds number.

Early investigations of this effect relied on simplified stochastic models (Levin and Sedunov 1966; Mazin 1968; Bartlett and Jonas 1972; Srivastava 1989; Cooper 1989). A more recent approach is the so-called large-eddy hopping, which follows the different growth histories of many different droplets arriving at a given point inside a cloud, each experiencing a different supersaturation history as a result of entrainment and mixing (Lasher-Trapp et al. 2005; Cooper et al. 2011; Bewley and Lasher-Trapp 2011). Previous cloud simulations have been performed by means of large-eddy simulations, a numerical technique consisting in modeling cloud turbulence by solving the filtered Navier–Stokes equations. This technique requires a subgrid-scale model for the smallest scales of turbulence. Several LES studies describe the problems of cloud droplet growth by condensation in the atmospheric boundary layers such as Magaritz-Ronen et al. (2014) and Riechelmann et al. (2015). In the last years, increased computing power has enabled brute-force approaches in which direct numerical simulation (DNS) of the Navier–Stokes equations is used to generate turbulent velocity and supersaturation fields within a cubic domain containing a large swarm of droplets that are individually tracked as Lagrangian particles and allowed to interact with the supersaturation field. Such technique aims to capture the effect of turbulence within a small subdomain of the adiabatic (nonentraining) core of a cumulus cloud and it does not require any subgrid model. The first study of this type (Vaillancourt et al. 2002) used 5×10^4 droplets in a domain of about $10\,\mathrm{cm}^3$ with a resolution of 80^3 grid points. The main conclusion of this study was that small-scale turbulence rapidly moves droplets from regions of high and low supersaturation, without a significant increase of the variance of the droplet size spectrum. On the other hand, focusing on the large-scale turbulence fluctuations in a cloud of 100-m size, Celani et al. (2007) found a dramatic broadening of the droplet spectrum, although the dynamics of the small scales was not resolved since the simulation Kolmogorov scale was unrealistically large. The same effect was reported in Paoli and Shariff (2009), where an artificial forcing term was added to the supersaturation equation to mimic the effect of the large-scale eddies.

Lanotte et al. (2009) addressed the issue of the relative roles of small- and large-scale eddies in broadening droplet size spectra. These authors performed a series of DNS simulations progressively increasing the range of resolved scales, keeping the Kolmogorov scale fixed but increasing the external scale up to 70 cm including over 3×10^7 droplets with initially identical sizes. They found that the spectra broadened as the simulation proceeded; crucially, the broadening achieved after a fixed time increased as the domain size (and thus the Reynolds number) increased. They also provided scaling arguments to suggest that this increase in spectral width can be extrapolated to higher Reynolds number as a power law. These results suggest that the broadening effect of large-scale eddies becomes increasingly dominant as Reynolds number increases. Nevertheless, this broadening effect is limited by the value of the quasi-equilibrium supersaturation s^{qs} as described in Grabowski and Wang (2013). In general, supersaturation fluctuations increase with the Reynolds number but cannot be larger than s^{qs}, which weakly depends on the characteristic turbulent scale L of the system ($s^{qs} \propto v_{rms} \propto L^{1/3}$ in the turbulent inertial range, where v_{rms} indicates a characteristic velocity at scale L).

In recent work (Sardina et al. 2015), we focused on the time evolution of the droplet size spectrum. Using a modeling setup similar to Lanotte et al. (2009) but with a domain size up to 3 m and longer simulation times, we found that the width of the droplet spectrum increases continuously in time as $t^{1/2}$. Further, we found that the broadening rate is linearly dependent on the ratio between the large and the small turbulent scales, that is, proportional to the Reynolds number. We also presented a simple stochastic model that quantitatively predicts the broadening rates in the numerical simulations and can be used to extrapolate to greater Reynolds numbers. A simplified version of our stochastic model, involving just the time evolution of the supersaturation field, was recently tested and experimentally validated in a laboratory cloud chamber (Chandrakar et al. 2016), showing excellent agreement between the model and experimental data. These results imply that the width of the droplet size distribution can become realistically large at any Reynolds number so long as one waits long enough; for realistic cloud Reynolds numbers, the time required is about 20 min. In the same context, new stochastic approaches have been developed more recently. Siewert et al. (2017) extended our stochastic model to the case where droplets are allowed to fully evaporate and also accounting for the variation of the supersaturation relaxation time. Grabowski and Abade (2017) formulated a new stochastic model aimed at improving subgrid-scale modeling in LESs.

For the sake of simplicity, Sardina et al. (2015) made several unrealistic assumptions. In particular, the cloudy parcel was assumed to be stationary, with a domain-mean supersaturation held fixed at zero. Also, the droplets were assumed to be initially monodisperse with a radius of 10 μm. Here, we extend our previous work by relaxing these assumptions, including the effect of a mean updraft velocity and examining activation of CCN of different composition. Given the current computational resources, studies involving CCN activation either include a complete representation of cloud turbulence while using a simple representation of cloud microphysics (Lasher-Trapp et al. 2005; Bewley and Lasher-Trapp 2011) or rely on simple methods for representing cloud turbulence using a more complete representation of the cloud microphysics (Jensen and Nugent 2017). Very few studies have addressed the question in simple homogeneous isotropic turbulence and for computational expedience used two-dimensional DNS (Celani et al. 2008, 2009).

Our modeling setup and assumptions are discussed in section 2. In section 3 we briefly review the results of Sardina et al. (2015) and elucidate the physical mechanisms underlying the time-dependent turbulent broadening. Section 4a considers the effect of a mean updraft velocity on the spectrum evolution of initially large droplets, while in section 4b we study the influence of droplet activation and deactivation by conducting simulations starting from cloud condensation nuclei. Finally, Section 5 presents a discussion and conclusions.

2. Model description

We aim to model a warm-cloud parcel occupying a domain of order $L = 100$ m, large enough to produce a large Reynolds number but still small enough to neglect the effects of spatial inhomogeneity and variations of the thermodynamic parameters within the domain so that a homogeneous, isotropic turbulence assumption is reasonable. Under these conditions the turbulent kinetic energy dissipation ε is typically of order 10^{-3} m^2 s^{-3} and the cloud Kolmogorov scale is $\eta = (\nu^3/\varepsilon)^{1/4} = 1$ mm, where ν is the kinematic viscosity of air. The computational domain is assumed to ascend with a constant updraft speed W with the macroscopic thermodynamic variables temperature $\langle T \rangle$ and pressure $\langle P \rangle$ evolving according to (Vaillancourt et al. 2002):

$$\frac{d\langle T \rangle}{dt} = -W\Gamma_d + \frac{\mathcal{L}}{c_p}\langle C_d \rangle \quad \text{and} \tag{1}$$

$$\frac{d\langle P \rangle}{dt} = -\rho g W, \tag{2}$$

with Γ_d the dry adiabatic lapse rate, $\mathcal{L}$ the latent heat of evaporation, c_p the specific heat at constant pressure, and $\langle C_d \rangle$ the condensation rate based on the mean droplet radius $\langle R \rangle$. The macroscopic pressure is modeled by the hydrostatic approximation with ρ as the air density g as the gravitational acceleration.

The underlying turbulence obeys the incompressible Navier–Stokes equations in homogeneous isotropic configurations while the supersaturation field s is transported by the fluid according to the Twomey model (Twomey 1959). Direct numerical simulation of the complete Navier–Stokes system from the large scales of order 100 m down to the Kolmogorov scale on the order of 1 mm is unfeasible with the current computational resources. In the following we will therefore focus on the larger-scale dynamics, directly resolving the large scales and modeling the small scales, an approach commonly denoted as "large-eddy simulation" (LES). The choice of employing LES is justified by previous work showing that the droplet condensation–evaporation dynamics in a turbulent flow is dominated by the large scales (Sardina et al. 2015). The LES equations read as follows:

$$\nabla \cdot \mathbf{u}' = 0, \tag{3}$$

$$\frac{\partial \mathbf{u}'}{\partial t} + \mathbf{u}' \cdot \nabla \mathbf{u}' = -\frac{\nabla p'}{\rho} + \nu \nabla^2 \mathbf{u}' - \nabla \cdot \boldsymbol{\tau}_{\text{sgs}} + \mathbf{f}_u', \quad \text{and} \tag{4}$$

$$\frac{\partial s}{\partial t} + \mathbf{u}' \cdot \nabla s = \kappa \nabla^2 s + A_1(\langle T \rangle)(w' + W) + \nabla j_{\text{sgs}} - \frac{s}{\tau_s}, \tag{5}$$

where $\mathbf{u}'$ is the resolved turbulent fluctuating velocity, p' the pressure fluctuations, $\mathbf{f}_u$ an external forcing able to maintain a statistically stationary state, κ the diffusivity of water vapor in air, s is the resolved turbulent fluctuating scalar field for supersaturation, w' is the component of the fluctuating velocity field acting in the gravity direction, $A_1(w' + W)$ is source/sink term of supersaturation resulting from the variation in temperature and pressure with height, τ_{sgs} is the so-called subgrid stress tensor that models the effect of the small scales on the large-scale dynamics, and j_{sgs} is the correspondent subgrid flux for the supersaturation field. We choose the simplest subgrid model, the Smagorinsky model (Smagorinsky 1963), for both τ_{sgs} and j_{sgs}; in this model the stress is proportional to an eddy viscosity, $\tau_{\text{sgs}} = -2\nu_t \mathbf{E}$, and $\nu_t = (c_s \Delta)^2 |\mathbf{E}|$ with c_s the Smagorinski constant, Δ the grid size, $|\mathbf{E}|$ the modulus of the rate of strain tensor, and $k_t = \nu_t/0.7$ the eddy diffusivity. The parameter τ_s is the relaxation time scale of the supersaturation field and depends on the droplet size and concentration (Kostinski 2009); this is locally calculated in each computational cell according to (Lanotte et al. 2009):

$$\tau_s^{-1} = 4\pi \rho_w A_2(\langle T \rangle, \langle P \rangle) A_3(\langle T \rangle) \sum R / V_{\text{cell}},$$

where R are the radii of the droplets in the numerical cell volume V_{cell}, ρ_w is the water density, and $A_1(\langle T \rangle)$, $A_2(\langle T \rangle, \langle P \rangle)$, and $A_3(\langle T \rangle)$ are functions of the macroscopic thermodynamic quantities $\langle T \rangle$ and $\langle P \rangle$ but weakly depend on their fluctuations inside the turbulent domain T' and p; see supplemental material in Sardina et al. (2015). They are calculated according to the following expressions (Pruppacher and Klett 1997) and change in time owing to the variation of $\langle T \rangle$ and $\langle P \rangle$ during the parcel ascent:

$$A_1(\langle T \rangle) = \frac{g\mathcal{L}}{\mathcal{R}_v c_p \langle T \rangle^2} - \frac{g}{\mathcal{R}_d \langle T \rangle}, \tag{6}$$

$$A_2(\langle T \rangle, \langle P \rangle) = \frac{\mathcal{R}_d \langle T \rangle}{\lambda e_s(\langle T \rangle)} + \frac{\lambda \mathcal{L}^2}{\langle P \rangle \langle T \rangle c_p}, \quad \text{and} \tag{7}$$

$$A_3(\langle T \rangle) = \left[\frac{\rho_w \mathcal{R}_v \langle T \rangle}{D_v e_s(\langle T \rangle)} + \frac{\rho_w \mathcal{L}^2}{k_T \mathcal{R}_v \langle T \rangle^2} \right]^{-1}, \tag{8}$$

with $\mathcal{R}_v$ and $\mathcal{R}_d$ the water vapor and dry-air gas constants, λ the ratio between water and dry-air molecular weights, $e_s(\langle T \rangle)$ the supersaturation pressure obeying Clausius–Clapeyron equation, D_v the thermal diffusivity of water vapor in air, and k_T the thermal diffusivity. Buoyancy effects in the momentum equation can be neglected at scales below 100 m according to the scaling arguments described in Vaillancourt and Yau (2000). Previous simulations of CCN growth in a turbulent field neglected the effect of the parameter τ_s (Celani et al. 2008),

whereas we consider the complete coupling between droplets and supersaturation field.

In general, droplet dynamics can be described by two different approaches: Lagrangian and Eulerian. In the Lagrangian approach, each droplet is tracked along its motion around the cloud. Equations for their position, velocity, and radius must be numerically solved, and particle–particle interactions and collisions can be described in a natural way (Paoli and Shariff 2009; Lanotte et al. 2009; de Lozar and Muessle 2016). The computational requirements of this approach using realistic droplet numbers can be prohibitive, so the use of a renormalization method or the so-called superdroplet approach is necessary (Shima et al. 2009). Alternatively, the droplet dynamics can be described following the Eulerian approach in terms of a conservation equation for the droplet distribution $f(\mathbf{x}, r, t)$ and the droplet velocity distribution $\mathbf{v}_d(\mathbf{x}, r, t)$. These equations need to be discretized in the radius space r and many terms require a closure model, especially if collisions are included. A review and a comparison between the two approaches can be found in the recent paper by Li et al. (2017).

We employ a Lagrangian framework in our simulations: under the hypothesis of small spheres with dimensions smaller than Kolmogorov scale and low mass fraction to neglect two-way coupling effects on the carrier flow, the only forces acting on the droplets are gravity and Stokes drag:

$$\frac{d\mathbf{v}_d}{dt} = \frac{\mathbf{u}(\mathbf{x}_d, t) - \mathbf{v}_d}{\tau_d} - g\mathbf{e}_z \quad \text{and} \tag{9}$$

$$\frac{d\mathbf{x}_d}{dt} = \mathbf{v}_d, \tag{10}$$

where $\mathbf{x}_d$ is the droplet position, $\mathbf{v}_d$ is the droplet velocity, $\mathbf{u}(\mathbf{x}_d, t)$ is the fluid velocity at droplet position, $\tau_d = 2\rho_w R^2/(9\rho\nu)$ is the droplet relaxation time, gravity is directed along the unit vector $-\mathbf{e}_z$, and $s(\mathbf{x}_d, t)$ is the supersaturation at the droplet position. Collisions among droplets are not considered.

Droplet activation and condensational growth is modeled using standard Köhler theory (Köhler 1936):

$$\frac{dR}{dt} = A_3 \frac{s(\mathbf{x}_d, t) - c/R + h/R^3}{R}. \tag{11}$$

The last two terms in the numerator of the right-hand side of Eq. (11) are only important when R is well below $5\,\mu\text{m}$, during the droplet activation stage. The term c/R accounts for the curvature or Kelvin effect: water molecules evaporate more readily from a large-curvature surface. The consequence is that homogeneous nucleation requires very

large supersaturation, so droplets preferentially form around CCN (often ionic salt aerosols) that have affinity with the water vapor (hygroscopicity). This solute or Raoult effect is represented by the second term, h/R^3. The curvature coefficient is $c = 2\sigma M_w/(\mathcal{R}\langle T\rangle\rho_w)$, while the hygroscopicity coefficient is defined as $h = 3n_s m_s M_w/(4\pi\rho_w M_s)$, where σ is the surface tension between water and air, $\mathcal{R}$ the universal gas constant, n_s the ion number for a specific salt, m_s the mass of the hygroscopic CCN, and M_w and M_s the water and the salt molar masses. A droplet is activated and grows spontaneously by condensation when its radius exceeds the critical value $R_c = \sqrt{3h/c}$, corresponding to the critical supersaturation $s_c = \sqrt{4c^3/(27h)}$. This model for droplet activation and condensation is the same of the two-dimensional DNS study of Celani et al. (2008). No subgrid model is assumed for the droplet Lagrangian equations since droplet evaporation/condensation is weakly influenced by the small-scale dynamics (under 1 m); see supplemental materials in Sardina et al. (2015). The impact of turbulence on condensational droplet growth is small at these small scales because the rapid rearrangement of droplet positions decorrelates the droplet from the underlying scalar field as shown in Vaillancourt et al. (2002) and described in Grabowski and Wang (2013). In general, however, a subgrid-scale model is required in LESs of real clouds with grid resolution on the order of meters to avoid inaccuracies in the droplet correlation with the underlying scalar field along droplet trajectories. A new multiscale subgrid model has been recently developed in Mazzitelli et al. (2014b) to model tracer dispersion and applied to convective boundary layer turbulence (Mazzitelli et al. 2014a). An alternative approach is the novel subgrid model introduced in Grabowski and Abade (2017).

We solve the Eulerian equations for the turbulent flow with a pseudospectral method on a uniform grid employing three-dimensional fast Fourier transforms. Time integration is performed with a low-storage third-order Runge–Kutta where the nonlinear terms are computed via an Adam–Bashforth-like approximation and the diffusive terms analytically integrated (Rogallo 1981). Nonlinear terms are classically computed in physical space and dealiased with a standard 2/3 rule. The same time integration scheme is used for the droplet evolution and a three linear interpolation/extrapolation scheme is used to estimate the variables from the Eulerian to the Lagrangian reference frames and vice versa. Droplet velocity and radius are integrated in time with an implicit scheme (predictor–corrector) (Olivieri et al. 2014) to avoid the use of a very small time step associated with a low droplet relaxation time and low values of the droplet radius. Note that, although included, we have verified that the effect of droplet inertia could be safely neglected for our parameter range. [The initial Stokes numbers of the simulations are shown in Table 2. The Stokes number is based on the Kolmogorov time scale $\tau_\eta = (\nu/\varepsilon)^{1/2} = 0.1$ s and assumes values well below 1 in all the cases considered in this manuscript.]

We performed 12 different simulations divided into three groups differing in the chemical composition of the initial salt nuclei. In particular we evolve (i) already-activated droplets with initial radius $R_0 = 13\,\mu m$ and no nucleus salt, (ii) $(NH_4)SO_4$ salt CCN with initial radius $R_0 = 0.24\,\mu m$, and (iii) NaCl salt CCN with initial radius $R_0 = 0.022\,27\,\mu m$. The chemical and physical properties of the three droplet populations are summarized in Table 1. For each droplet family we perform four simulations differing in the updraft velocity W, spanning the range from 0 to $1\,m\,s^{-1}$. Each simulation uses a mesh of 256^3 grid points with 70 million droplets. A droplet renormalization method is employed to achieve an equivalent concentration of 130 droplets per cubic centimeter and to keep at least 3–6 droplets per computational cell (Lanotte et al. 2009). The renormalization procedure is necessary since we cannot evolve each single droplet inside a 100-m cloud with the actual computational resources (10^{14} droplets in our case). A renormalization factor of 2×10^6 has been used in our simulations. The use of a renormalization approach is commonly used in the superdroplet method to account the droplet–droplet collisions; the renormalization factor is also called multiplicity. Each simulation is integrated up to a final time of 20 min and is characterized by a root-mean-square turbulent velocity fluctuation of $0.7\,m\,s^{-1}$, an integral time scale T_0 of 33 s, and a Taylor Reynolds number (Re_λ) of 5000. The time step is 0.03 s, the initial temperature is 288 K, the initial average supersaturation $\langle s^0\rangle$ is zero while its root-mean-square is $s^0_{rms} = 1\%$. This last value was obtained by running a spinup simulation without the presence of the droplets for 100 s. The different Eulerian and Lagrangian turbulent parameters are summarized in Table 1. The particles are assumed to be initially monodisperse, with diameters reported in Table 2. The effects of the initial radius size spectrum can be investigated in future studies.

3. Broadening of the droplet size distribution

In this section, we extend the main results of our previous study (Sardina et al. 2015). In Sardina et al. (2015), we conducted DNSs and LESs using the same model used here (see section 2) with updraft $W = 0$ and neglecting the Kelvin and Raoult terms in Eq. (11), initializing the simulations with droplets large enough to ensure that they remained well above the critical

TABLE 1. Parameters of the numerical simulations for the turbulent gas flow: L_{box}, cloud size; Δ, numerical resolution; Re_λ, Taylor Reynolds number; ε, turbulent kinetic energy dissipation; v_{rms}, turbulent velocity fluctuations; T_L, Eulerian large-eddy turn over time; T_0, Lagrangian integral time; $\langle s^0 \rangle$, initial average supersaturation field; s^0_{rms}, initial supersaturation root-mean-square; N_d, number of droplets inside the cloud; N_c, number of representative droplets evolved in the simulation.

L_{box} (m)	Δ (m)	Re_λ	ε (m² s⁻³)	v_{rms} (m s⁻¹)	T_L (s)	T_0 (s)	$\langle s_0 \rangle$	s^0_{rms} (%)	N_d	N_c
100	0.39	5000	10^{-3}	0.7	142	33	0	1	10^{14}	7×10^7

activation radius at all times. We also derived a simple stochastic model able to accurately reproduce the time evolution of the droplet size spectrum. As in the present work, we did not consider entrainment (Kumar et al. 2014), collisions, or inhomogeneity, so that the size spectrum evolution is driven only by the supersaturation fluctuations.

In the stochastic model of Sardina et al. (2015) the turbulent vertical velocity and supersaturation fluctuations are modeled using Langevin equations (Pope 2000). Here we will include the effect of a mean supersaturation field following the approach by Paoli and Shariff (2009). The modified stochastic model reads as follows:

$$w'_i(t + dt) = w'_i(t) - \frac{w'_i(t)}{T_0} dt + v_{rms} \sqrt{2 \frac{dt}{T_0}} \xi_i(t) \quad \text{and} \quad (12)$$

$$s_i(t + dt) = s_i(t) - \frac{s_i - \langle s \rangle}{T_0} dt + A_1(W + w'_i) dt$$
$$- \frac{4\pi \rho_w A_2 n}{3} dR^3 + \sqrt{(1 - C^2_{ws})\langle s'^2 \rangle \frac{2dt}{T_0}} \eta_i(t)$$
$$+ C_{ws} \sqrt{\langle s'^2 \rangle \frac{2dt}{T_0}} \xi_i(t), \quad (13)$$

where v_{rms} is the standard deviation of the turbulent velocity fluctuations, $\xi(t)$ and $\eta(t)$ Gaussian δ correlated in time white noise, T_0 the turbulence integral time scale, $C_{ws} = \langle w's' \rangle / (v_{rms}\sqrt{\langle s'^2 \rangle})$ the normalized velocity–supersaturation correlation, n is the droplet concentration, $\langle s \rangle$ is the average supersaturation, and $\langle s'^2 \rangle$ its variance. This system is coupled with the equation for the evolution of the droplet radius, Eq. (11).

The time evolution of the square droplet radius standard deviation σ_{R^2} follows the exact equation:

$$\frac{d\langle (R_i^{2\prime})^2 \rangle}{dt} = \frac{d\sigma^2_{R^2}}{dt} = 4A_3 \langle s' R^{2\prime} \rangle. \quad (14)$$

The previous equation highlights the role of the correlation $\langle s'R^{2\prime} \rangle$ in modifying the droplet spectral distribution. This quantity, derived analytically, represents the covariance between the droplet surface and the supersaturation fluctuations. Physically, the key parameter that accounts for the role of turbulence in droplet condensation is this statistical observable. If the covariance is large and positive, a large spectral broadening is possible even in absence of collisions. In the following we will derive a closure model for this quantity based essentially on the values of the quasi-equilibrium supersaturation and the turbulent integral time scale. Another similar closure of this important term has been proposed by Chandrakar et al. (2016) and compared with experimental data in a cloud chamber. By manipulating and making approximations into the stochastic equations above, we can estimate the value of the correlation $\langle s'R^{2\prime} \rangle$ and consequently the square droplet radius standard deviation σ_{R^2}. The first step is to approximate the sink term proportional to dR^3 as a function of the square droplet radius R^2. We will assume that the deviation of the single droplet squared radius R^2 from its average value $\langle R^2 \rangle$ is small so that we can expand R^3 in Taylor's series:

$$R^3 = (R^2)^{3/2} \simeq \langle R^2 \rangle^{3/2} + \frac{3}{2}\langle R^2 \rangle^{1/2}(R^2 - \langle R^2 \rangle), \quad (15)$$

and differentiating,

TABLE 2. Parameters defining the CCN of the present simulations: critical radius and critical supersaturation depending on the salt composition and initial supersaturation relaxation time.

Salt	R_0 (μm)	St^0_η	c (nm)	h (μm³)	R_c (μm)	s_c (%)	τ^0_s (s)
—	13	0.03	—	—	—	—	2.3
$(NH_4)SO_4$	0.24	10^{-3}	1.2	9.8×10^{-3}	4.95	1.6×10^{-2}	124
NaCl	0.02227	10^{-7}	1.2	1.35×10^{-5}	0.18	0.43	1340

$$dR^3 = \langle R^2 \rangle^{1/2} \left(-\frac{3}{4} d\langle R^2 \rangle + \frac{3}{4} \frac{R^2}{\langle R^2 \rangle} d\langle R^2 \rangle + \frac{3}{2} dR^2 \right). \quad (16)$$

The evolution of the square droplet radius R^2 and its average quantity $\langle R^2 \rangle$ can be obtained by Eq. (11) neglecting the Raoult and Kelvin terms (active droplets):

$$\frac{dR^2}{dt} = 2A_3 s \quad \text{and} \quad (17)$$

$$\frac{d\langle R^2 \rangle}{dt} = 2A_3 \langle s \rangle \quad (18)$$

and substituting in Eq. (16),

$$dR^3 = \langle R^2 \rangle^{1/2} \left(-\frac{3}{2} A_3 \langle s \rangle + \frac{3}{2} \frac{R^2}{\langle R^2 \rangle} A_3 \langle s \rangle + 3A_3 s \right) dt. \quad (19)$$

Using Eq. (19) and defining the average droplet saturation time as $\langle \tau_s \rangle = (4\pi \rho_w A_2 A_3 n \langle R^2 \rangle^{1/2})^{-1}$, the stochastic supersaturation equation [Eq. (13)] assumes the following form:

$$s_i(t + dt) = s_i(t) - \frac{s_i - \langle s \rangle}{T_0} dt + A_1(W + w_i') \, dt$$

$$- \frac{dt}{\langle \tau_s \rangle} \left[\frac{\langle s \rangle}{2} \left(\frac{R_i^2}{\langle R^2 \rangle} - 1 \right) + s_i \right]$$

$$+ \sqrt{(1 - C_{ws}^2)\langle s'^2 \rangle \frac{2dt}{T_0}} \eta_i(t)$$

$$+ C_{ws} \sqrt{\langle s'^2 \rangle \frac{2dt}{T_0}} \xi_i(t). \quad (20)$$

Equation (20) can be decomposed in the evolution of the ensemble-average supersaturation,

$$\frac{d\langle s \rangle}{dt} = A_1 W - \frac{\langle s \rangle}{\langle \tau_s \rangle}, \quad (21)$$

and its fluctuating value,

$$s_i'(t + dt) = s_i'(t) - \frac{s_i'}{T_0} dt + A_1 w_i' dt - \frac{dt}{\langle \tau_s \rangle} \left(\frac{\langle s \rangle}{2} \frac{R_i^{2'}}{\langle R^2 \rangle} + s_i' \right)$$

$$+ \sqrt{(1 - C_{ws}^2)\langle s'^2 \rangle \frac{2dt}{T_0}} \eta_i(t) + C_{ws} \sqrt{\langle s'^2 \rangle \frac{2dt}{T_0}} \xi_i(t). \quad (22)$$

Assuming $\langle \tau_s \rangle \ll T_0$, the time evolution of the fluctuation correlations become

$$\frac{d\langle s'R^{2'} \rangle}{dt} = A_1 \langle w'R^{2'} \rangle + 2A_3 \langle s'^2 \rangle - \frac{\langle s'R^{2'} \rangle}{\langle \tau_s \rangle} - \frac{\langle s \rangle}{2\langle \tau_s \rangle} \frac{\langle R^{2'2} \rangle}{\langle R^2 \rangle}, \quad (23)$$

$$\frac{d\langle w'R^{2'} \rangle}{dt} = 2A_3 \langle w's' \rangle - \frac{\langle w'R^{2'} \rangle}{T_0}, \quad (24)$$

$$\frac{d\langle s'^2 \rangle}{dt} = 2A_1 \langle w's' \rangle - 2\frac{\langle s'^2 \rangle}{\langle \tau_s \rangle} - \frac{\langle s \rangle}{\langle \tau_s \rangle} \frac{\langle s'R^{2'} \rangle}{\langle R^2 \rangle}, \quad \text{and} \quad (25)$$

$$\frac{d\langle w's' \rangle}{dt} = A_1 v_{rms}^2 - \frac{\langle w's' \rangle}{\langle \tau_s \rangle} - \frac{\langle s \rangle}{2\langle \tau_s \rangle} \frac{\langle w'R^{2'} \rangle}{\langle R^2 \rangle}. \quad (26)$$

Unfortunately, the system of Eqs. (23)–(26) cannot be analytically solved for the most general case. The problem is simplified in the case of zero mean supersaturation $\langle s \rangle = 0$ and assuming a statistical quasi-steady state $(d\langle \cdot \rangle/dt = 0)$. Under these hypotheses we retrieve the theoretical results of our previous paper (Sardina et al. 2015). In particular, the correlation $\langle s'R^{2'} \rangle$ and consequently the distribution of squared droplet radius R^2 in time evolve according to the following expressions:

$$\langle s'R^{2'} \rangle = 2A_3 s^{qs2} T_0 = 2A_3 A_1^2 v_{rms}^2 \langle \tau_s \rangle^2 T_0 \quad \text{and} \quad (27)$$

$$\sigma_{R^2} = 2A_3^{1/2} \langle s'R^{2'} \rangle^{1/2} t^{1/2} = \sqrt{8} A_3 s^{qs} (T_0 t)^{1/2}$$

$$= \sqrt{8} A_3 A_1 v_{rms} \langle \tau_s \rangle (T_0 t)^{1/2}$$

$$\simeq 0.7 A_3 A_1 \nu^{1/2} \langle \tau_s \rangle \text{Re}_\lambda t^{1/2}. \quad (28)$$

Equation (28) shows that σ_{R^2} monotonically increases in time as $t^{1/2}$ and that the growth rate is proportional to the average relaxation time $\langle \tau_s \rangle$ and to the Taylor Reynolds number Re_λ, which is related to the large-to-small-scale separation. The spectral broadening captured by σ_{R^2} is bounded at a fixed time by the quasi-equilibrium supersaturation value $s^{qs} = A_1 v_{rms} \langle \tau_s \rangle$ consistently with the arguments of Lanotte et al. (2009) and Grabowski and Wang (2013). Furthermore, Eq. (28) extends their argument since σ_{R^2} scales with both s^{qs} and the turbulence integral scale T_0. In the turbulent inertial range, s^{qs} scales with $L^{1/3}$ and $T_0^{1/2}$ with $L^{1/3}$ and consequently σ_{R^2} scales as $L^{2/3}$, highlighting the importance of the large turbulent scales on the condensational growth.

A further key implication of Eq. (28) is that in the absence of an updraft velocity, the droplet size spectrum will continuously broaden in time, as discussed in our previous work (Sardina et al. 2015). The essence of this result can be understood by rewriting Eq. (11), neglecting the Kelvin and Raoult terms, as

$$\frac{dR^2}{dt} = 2A_3 s \quad (29)$$

and assuming that s behaves approximately as a white-noise process; in this case, R^2 performs a random walk and its standard deviation therefore increases as the square root of time. To visualize this behavior, the left
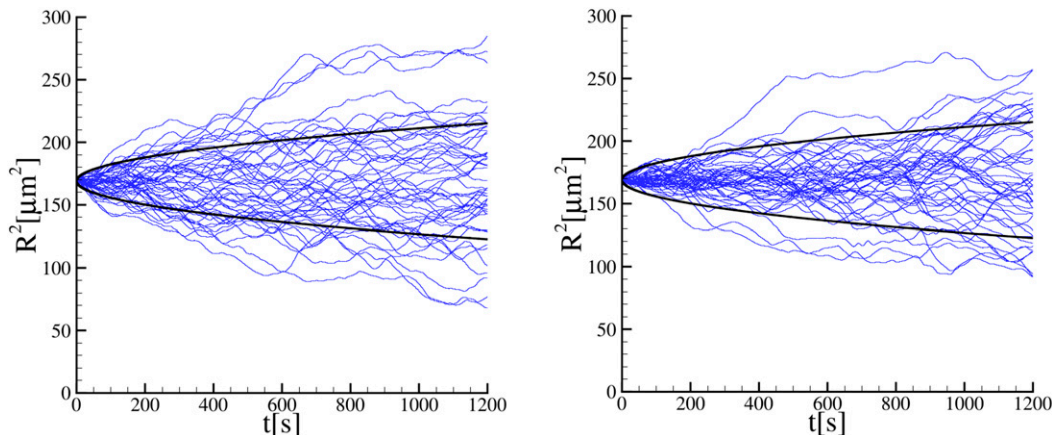
FIG. 1. Time evolution of the squared radius for 50 different individual droplets obtained with (left) the stochastic model and (right) LES. The black solid lines represent the evolution of the standard deviation.

panel in Fig. 1 shows the evolution of R^2 in numerical integrations of the stochastic model for 50 individual droplets along with the population standard deviation (which behaves as $t^{1/2}$) represented by the black line. All droplets have an initial radius $R = 13 \, \mu m$ but the stochastic fluctuations induce a dispersion in the radii that grows in time. The same qualitative behavior is obtained with the full turbulent 3D numerical simulations as shown in the right panel of Fig. 1, which again shows the evolution of 50 individual droplets starting from the same radius.

The analytical result above is limited by the droplet size, especially when the droplets are small as shown recently by Siewert et al. (2017). Our theoretical model assumes any possible value for the variable subjected to random walk R^2; however, the droplet squared radius cannot become negative by definition and a boundary condition should be included in the model. The quantity R^2 can be prescribed to be always positive as in Siewert et al. (2017) or subject to activation/deactivation (the Köhler effect) as we do in the present manuscript. In both cases, the particle size distribution reaches a steady state even without updraft velocity since the continuous broadening by condensation is limited for small values of R^2. Our stochastic model can therefore be used as a subgrid-scale model for the unresolved supersaturation in large-eddy simulation using a similar approach developed in Grabowski and Abade (2017).

4. Results

In this section we examine how the results described in the previous section change when a constant mean updraft $W > 0$ is introduced and when the droplet radii are allowed to drop below the critical radius so that droplet activation and deactivation become important.

a. Effect of mean updraft velocity

The presence of a mean updraft velocity induces several changes in the numerical and theoretical results shown in the previous section. The most obvious difference is that a mean updraft induces positive mean supersaturation inside the parcel and consequently a growing mean droplet radius. The top row of Fig. 2 shows the time evolution of the mean supersaturation field and of the mean radius for the sequence of runs initialized with a monodisperse droplet population (top row in Table 2). In all cases with $W > 0$, after an initial transient adjustment the mean supersaturation settles on a positive steady value in which the production of supersaturation by mean ascent [second term on the rhs of Eq. (5)] is balanced in the mean by condensation onto cloud droplets [last term on the rhs of Eq. (5)]. Droplets are on average gaining mass, and their mean radius increases monotonically (Fig. 2, top right). The $W = 0$ case is a little more subtle. In this case, mean supersaturation settles on a value just above zero; this is because the curvature term in the Köhler equation [Eq. (11)] increases the equilibrium vapor pressure slightly. There is no mean production of supersaturation and there is no mean change in total liquid water. Somewhat surprisingly, however, the mean droplet radius decreases over time.

The bottom panels of Fig. 2 show the time behavior of the supersaturation standard deviation (bottom left) and the ratio between mean and standard deviation of the supersaturation distribution (bottom right). For the chosen parameters, the supersaturation standard deviation depends weakly on the updraft velocity, decreasing slightly with the intensity of the updraft. This decrease is consistent with the stochastic model. The last term on the right-hand side of Eq. (25) is responsible of this small difference. Nonetheless, the quasi-steady
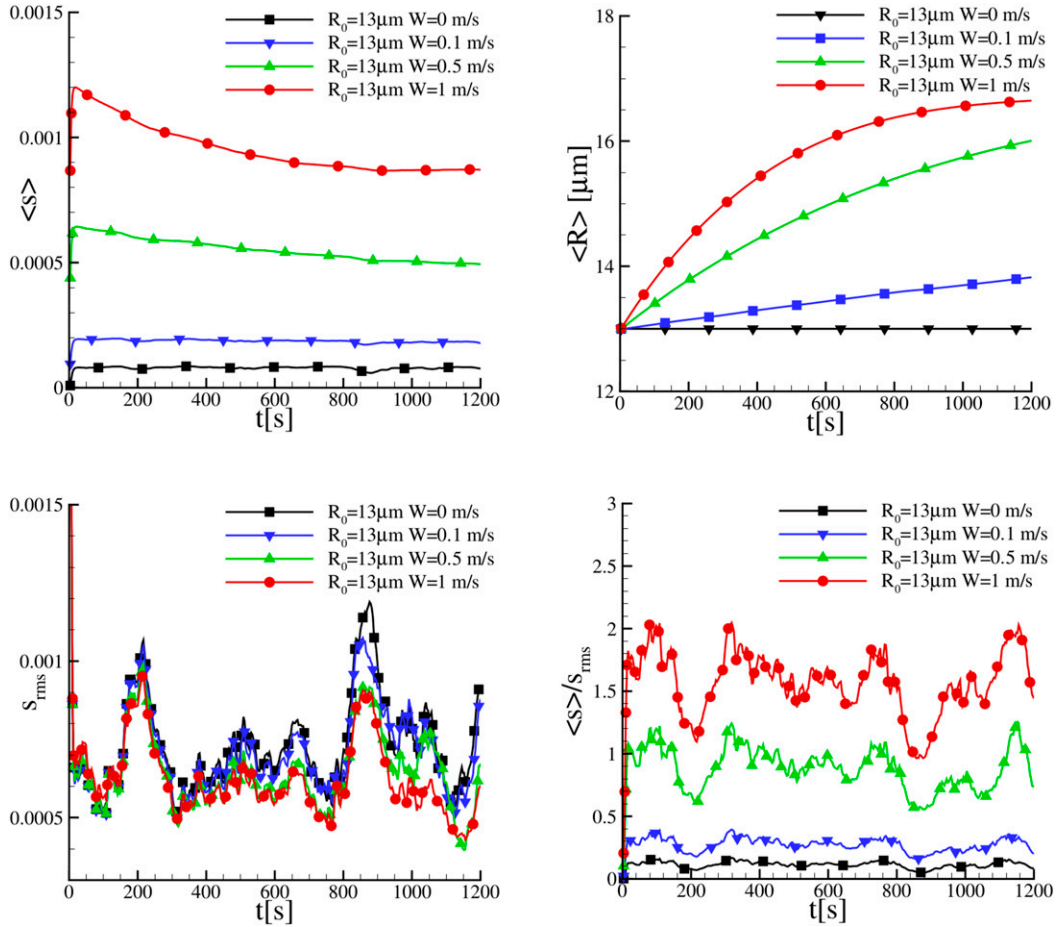
FIG. 2. Temporal evolution of (top left) mean cloud supersaturation, (top right) mean droplet radius, (bottom left) supersaturation standard deviation, and (bottom right) ratio between mean and standard deviation supersaturation for the largest droplets.

approximation $s_{\mathrm{rms}}^{\mathrm{qs}} = A_1 v_{\mathrm{rms}} \langle \tau_s \rangle$ obtained without updraft still provides a good estimate even for the larger updraft velocity that we are analyzing. The decrease of the supersaturation standard deviation with the updraft velocity is linked to the decrease of the supersaturation relaxation time $\langle \tau_s \rangle$ associated with the mean radius growth during ascent. The ratio between the mean and standard deviation of supersaturation oscillates around a steady mean value ranging from 0 for the zero updraft to 1.5 for the highest updraft velocity. These values will be useful to quantify the different behaviors of the droplet distributions.

The squared-radius distributions at the final simulation time, corresponding to 20 min, are shown in the top-left panel of Fig. 3. The distributions are approximately Gaussian for all the values of W, with skewness and kurtosis close to 0 and 3, respectively (bottom row). Note however that all distributions actually have a slight negative skewness, especially that for $W = 0$; indeed, the

distributions become more symmetric as W increases. The time evolution of the distributions' standard deviation is displayed in the top-right panel of Fig. 3. As in Sardina et al. (2015), the standard deviation grows approximately as $t^{1/2}$ in the case with no updraft. As the updraft strength increases, the growth becomes slower, apparently reaching a steady value in the $W = 1 \, \mathrm{m \, s^{-1}}$ case. The key result here, then, is that the presence of an updraft tends to counteract turbulent broadening and leads to a narrower droplet size distribution, in agreement with other recent work (Gotoh et al. 2016). This effect is confirmed by observing the correlation between the squared-radius fluctuations and the supersaturation fluctuations $\langle s' R^{2'} \rangle$. The time derivative of the squared-radius variance is proportional to the value of this correlation, $d\sigma_{R^2}^2 / dt \propto \langle s' R^{2'} \rangle$, which is therefore shown in Fig. 4. This has been shown in Sardina et al. (2015) to be constant in the absence of updraft. This observable then decreases by increasing the updraft velocity, being two
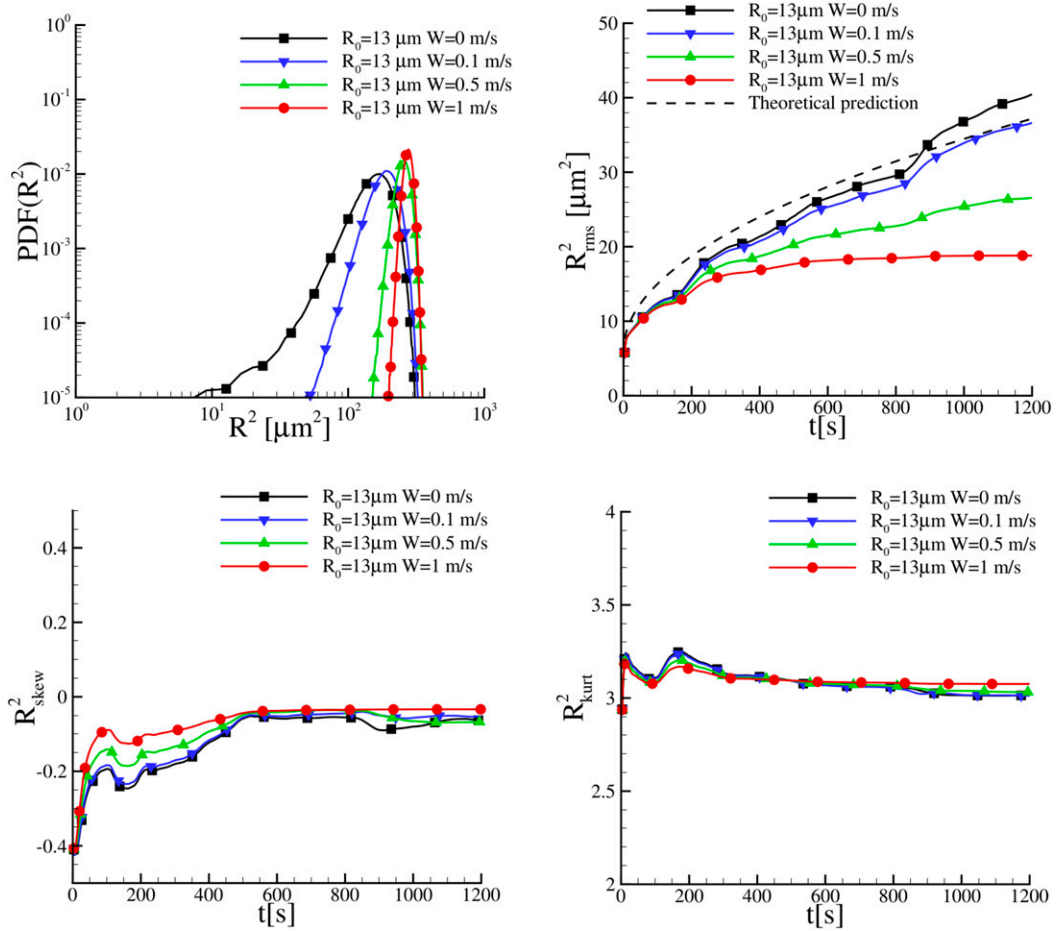
FIG. 3. (top left) Squared droplet radii pdf after 20 min of simulation for the largest droplets. Temporal evolution of squared droplet radius (top right) standard deviation, (bottom left) skewness, and (bottom right) kurtosis for the largest droplets.

orders of magnitude lower for the largest updraft case. The value of $\langle s'R^{2'}\rangle$ is almost constant in time for moderate updraft, implying that $\sigma_{R^2} \propto t^{1/2}$ while strongly diminishes at $W = 1\,\mathrm{m\,s^{-1}}$ in the last 400 s leading to the steady droplet spectrum distribution shown above. Thus, a strong updraft velocity tends to decorrelate the radius growth from the local resolved supersaturation field at the droplet position. The same conclusion can be reached by analyzing the time evolution of the correlation $\langle s'R^{2'}\rangle$ in the stochastic model [Eq. (23)], where again the last term on the right-hand side (which is negative if $\langle s\rangle > 0$) diminishes the value of the correlation. If we assume that the correlation $\langle s'R^{2'}\rangle$ tends to zero at large times, we can estimate an upper limit for the squared-radius standard deviation σ_{R^2}. In this case, the standard deviation asymptotically approaches a constant value in time—similarly to what observed in the simulations (Fig. 3, top right)—which can be approximated by

$$\sigma_{R^2} = \sqrt{\langle R^{2'2}\rangle} = \sqrt{(A_1\langle w'R^{2'}\rangle + 2A_3\langle s'^2\rangle)\frac{2\langle \tau_s\rangle\langle R^2\rangle}{\langle s\rangle}}.$$

(30)

If we assume again that the statistical steady state is reached, and that $T_0 \gg \tau_s$, the upper limit for σ_{R^2} becomes

$$\sigma_{R^2} = \sqrt{\langle R^2\rangle 4A_3 T_0 \frac{s_{\mathrm{rms}}^{\mathrm{qs2}}}{\langle s\rangle}} = \sqrt{\langle R^2\rangle 4A_3 T_0 \frac{A_1^2 v_{\mathrm{rms}}^2\langle \tau_s\rangle^2}{\langle s\rangle}} \propto \frac{\mathrm{Re}_\lambda}{\langle s\rangle^{1/2}}.$$

(31)

Equation (31) suggests that the final value of the spectral broadening depends on both the underlying turbulence Re_λ and the average supersaturation value $\langle s\rangle$. A positive mean supersaturation tends to reduce the spectral broadening. Again, the large turbulent scales play a fundamental role in determining the final stage of the
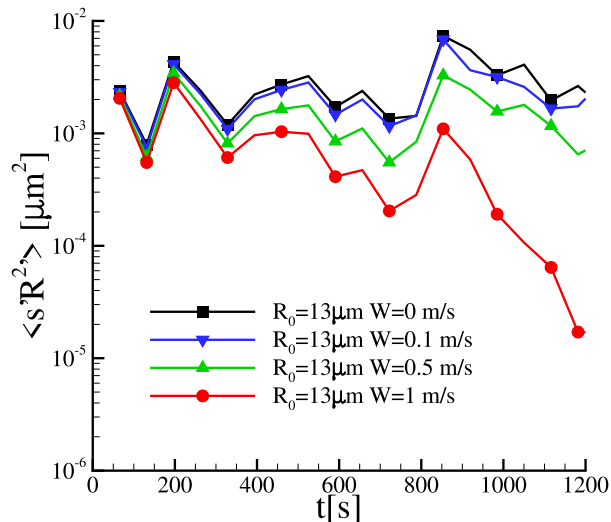
FIG. 4. Correlation between the squared-radius fluctuations and the supersaturation fluctuations $\langle s'R^{2'}\rangle$ for the largest droplets at different velocity updrafts.

droplet size distribution. The expression above confirms the limited droplet broadening found in the simulations by Vaillancourt et al. (2002) where a small turbulence level was simulated in a parcel ascending at $2.5\,\mathrm{m\,s^{-1}}$. Substituting in (31) the values used in the simulation, we obtain the upper limit $\sigma_{R^2} \simeq 30\,\mu\mathrm{m}^2$, indeed of the same order of magnitude of the simulation statistics at large times, $\simeq 20\,\mu\mathrm{m}^2$.

b. The role of droplet activation/deactivation

In the simulations presented in the previous section, the particles have been assumed to have an initial radius of $13\,\mu\mathrm{m}$ and no droplets came close to the critical activation radius in any of the simulations. Now, we show how the condensation dynamics can change when starting directly from CCN. We analyze two populations: ammonium sulfate $[(\mathrm{NH_4})\mathrm{SO_4}]$ and sodium chloride (NaCl). The two populations differ in chemical and physical properties and, consequently, critical activation radius and critical supersaturation.

The time evolution of the mean supersaturation and mean droplet radius are shown in the top-left and top-right panels of Fig. 5, respectively, for the case of $(\mathrm{NH_4})\mathrm{SO_4}$. The Kölher terms induce nonlinear effects for small radii, which prevents the droplet to evaporate in a negative supersaturation field in the absence of updraft. The mean radius is almost constant in time, around a value of $2\,\mu\mathrm{m}$. By increasing the updraft velocity, the mean radius starts to grow similarly to the case without CCN. The time evolution of the supersaturation standard deviation is shown in the bottom-left panel for all simulations. The values plotted in the figure can be

roughly estimated by using the quasi-equilibrium prediction $s_{\mathrm{rms}}^{\mathrm{qs}} = A_1 v_{\mathrm{rms}}\langle\tau_s\rangle$ with the average value of $\langle\tau_s\rangle$ calculated by means of the average radius plotted in the top-right panel of Fig. 5. The fluctuations of the supersaturation field decrease by more than one order of magnitude from zero to the highest updraft considered. The ratio between the mean and standard deviation of the supersaturation field, displayed in the bottom-right panel of Fig. 5, is quantitatively the same as in the case without CCN for the two largest updraft values.

The final droplet size distribution is shown in the top-left panel of Fig. 6. Two completely different behaviors emerge. For the largest updrafts, the pdfs are Gaussian, whereas the distributions depart consistently from the Gaussian distribution for the smallest updrafts. In the latter cases, the pdfs show a "haze peak" in correspondence to the critical CCN radius. The pdf pertaining to the case of zero updraft is qualitatively similar to that found in simulations of two-dimensional turbulence (Celani et al. 2008) and the distribution embraces a scale interval of more than two decades even for an updraft of $0.1\,\mathrm{m\,s^{-1}}$, with long and persistent tails. For the cases of higher updraft, we observe a saturation in time of the distribution for the $1\,\mathrm{m\,s^{-1}}$ updraft velocity as revealed by the time evolution of the distribution moments shown below. This can be of fundamental importance to estimate the droplet collision dynamics. We therefore examine the moments of the pdfs and report the standard deviation in the top-right panel of Fig. 6. Interestingly, the case with zero updraft substantially differs from the previous simulation with large droplets. Here, we observe a saturation of the droplet size standard deviation in time rather than a monotonic increase. On the other hand, the monotonic behavior in time can be observed for the intermediate updraft velocities. Since the cases with lower updraft velocities show highly non-Gaussian pdfs, the standard deviation does not give enough information on the droplet size spectrum. Figure 6 also shows the skewness (bottom left) and kurtosis (bottom right) of the size spectrum versus time. The data for the higher updraft values confirm that the droplet sizes have an almost Gaussian distribution since their skewness and kurtosis are about 0 and 3, respectively, like a pure Gaussian distribution. A positively skewed distribution is instead found for the two smaller updrafts examined. The positive value of skewness implies the presence of a right tail in the pdf and the lack of symmetry in the spectrum distribution. After time $t \approx 500\,\mathrm{s}$, the pdf has high kurtosis in the zero-updraft case, revealing the presence of large tails and that the droplet distribution reaches a steady state. The high value of kurtosis is about 3 times bigger than the one of the Gaussian distribution, implying that the pdf
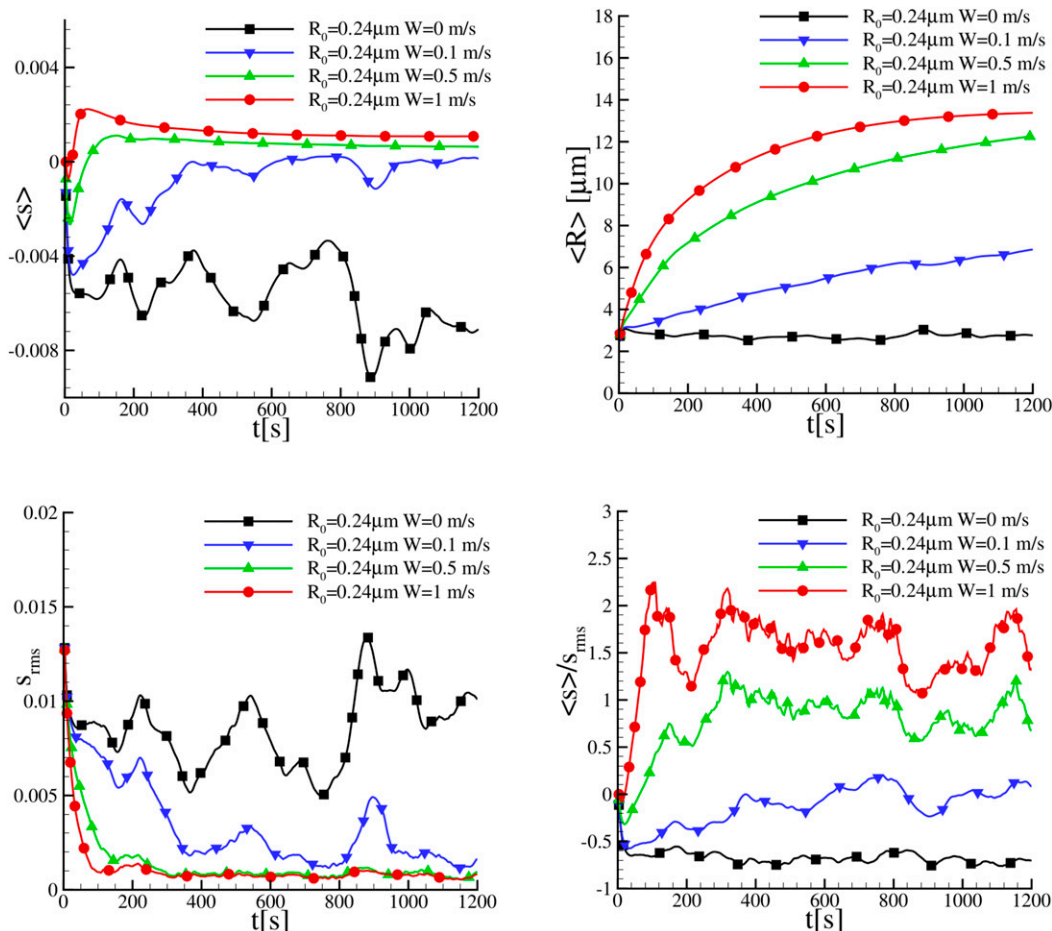
FIG. 5. Temporal evolution of (top left) mean cloud supersaturation, (top right) mean droplet radius, (bottom left) supersaturation standard deviation, and (bottom right) ratio between mean and standard deviation supersaturation for $(NH_4)SO_4$ salt CCN.

tails are persistent and decay slowly compared to the Gaussian one. The presence of this long and not symmetric right tail could be crucial for the following gravitational collisional stage of rain formation.

 The results for the case of the aerosol marine salt (NaCl) are depicted in Fig. 7: the main findings are consistent with those for the $(NH_4)SO_4$ aerosols discussed in Fig. 5. The only exceptions are found for the zero-updraft case where the water droplets are smaller in size and thus more dependent on the chemical composition of their nucleus. However, although the global supersaturation and average radius are similar for the two aerosol populations, the droplet size distribution is completely different, as shown in Fig. 8. The droplet size spectrum is shown in the top-left panel, where it is possible to distinguish three different regions: (i) The haze region around the droplet activation radius shows a very clear peak for all the updrafts considered. The peak is more pronounced and

distinguished from that in the case of $(NH_4)SO_4$ nuclei and clearly divides the nonactive from the active particles. The pdf of the nonactive droplets decays as a power law when decreasing the droplet dimensions; the exponent of the power law is around 1.5. (ii) An intermediate zone, characterized by a plateau in the size distribution, defines the active droplets up to 2–3 μm. (iii) For larger particles, those less influenced by their nucleus chemical composition, the droplet distribution recovers the behavior of the population considered previously. It is remarkable that, in this case, there is a difference of about six orders of magnitude between the squared radii of the larger and smaller droplets, to which corresponds the same variation in droplet terminal velocity with obvious consequences for collision rates. This broad spectrum appears for all the updraft velocities under consideration, with the larger updrafts showing a more distinct bimodal behavior. The previous observations are reflected in the high values of
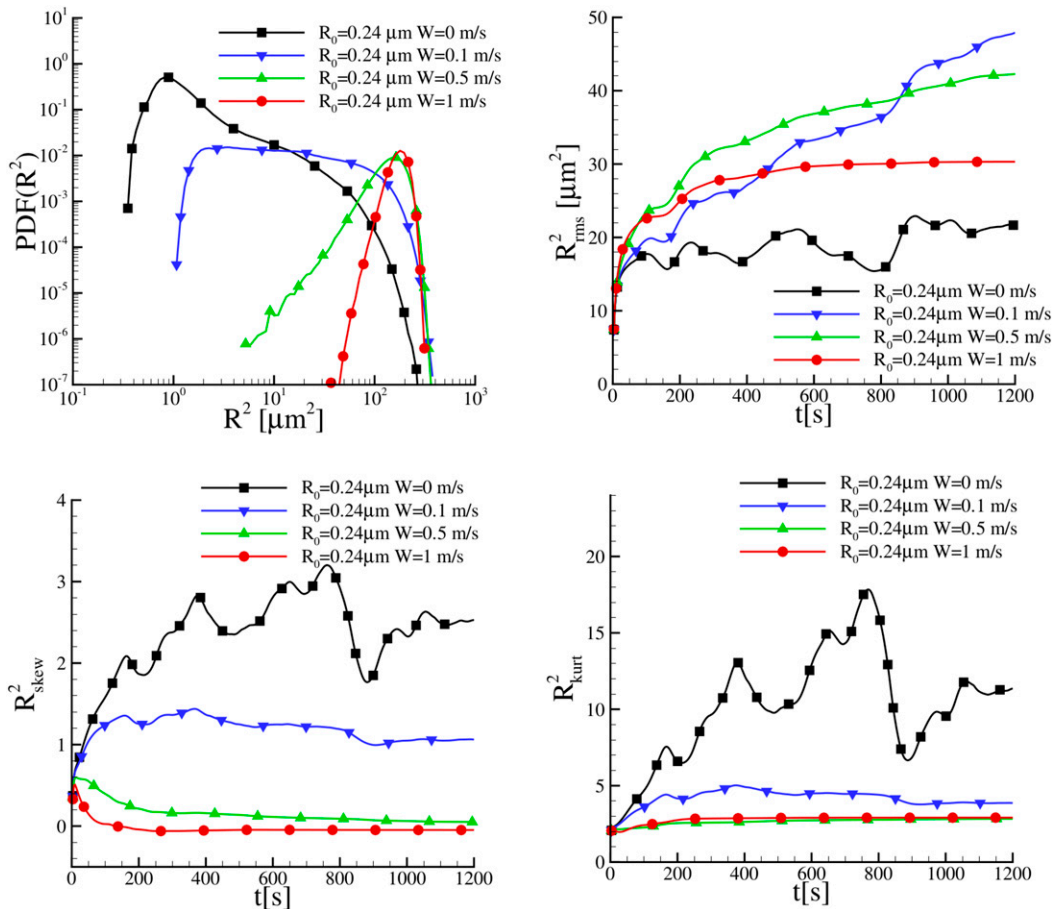
FIG. 6. (top left) Squared droplet radii probability density function pdf after 20 min of simulation for $(NH_4)SO_4$ salt CCN. Temporal evolution of squared droplet radius (top right) standard deviation, (bottom left) skewness, and (bottom right) kurtosis for $(NH_4)SO_4$ salt CCN.

the rms of R^2 reported in the top-right panel of Fig. 8. Since we consider in this case droplets of smaller radius, the zero-updraft distribution has not yet reached the steady state and its standard deviation continues to increase at the final simulation time; we believe the steady state will be reached at a later time. The loss of a quasi-Gaussian pdf at the larger updrafts is measured by the skewness of the distribution (bottom left panel): indeed, larger updrafts show a negatively skewed distribution in the droplet size spectra. High values of the kurtosis are also evident in almost all cases.

For the results just presented, we initially assumed the particle radius to be the radius of the salt condensation nucleus. We did several tests only changing the value of the initial droplet radius, from the activation radius to $5\,\mu m$ and, surprisingly, obtained the same results. These results are therefore dependent only on the chemical composition of the condensation nuclei and independent on the initial radius distribution. This

effect is a consequence of the initial conditions of the supersaturation field. The initial field is generated without the presence of the droplets and it is characterized by a larger standard deviation (1%). When the CCN are injected, many of them are activated instantaneously depending only of the value of c and h and the average radius of the droplet is on the order of $2–3\,\mu m$. For these reasons, the effect of the aerosol size is subleading. We understand that the choice of the initial condition can be arbitrary but our initial conditions are not so far from the recent experiments measures by Siebert and Shaw (2017). These authors found that at the early stages of cloud formation the fluctuations of the supersaturation are observed to be approximately normally distributed with standard deviations on the order of 1%. This variability is almost one order of magnitude larger than the steady-state value of the supersaturation as we also find in our numerical results.
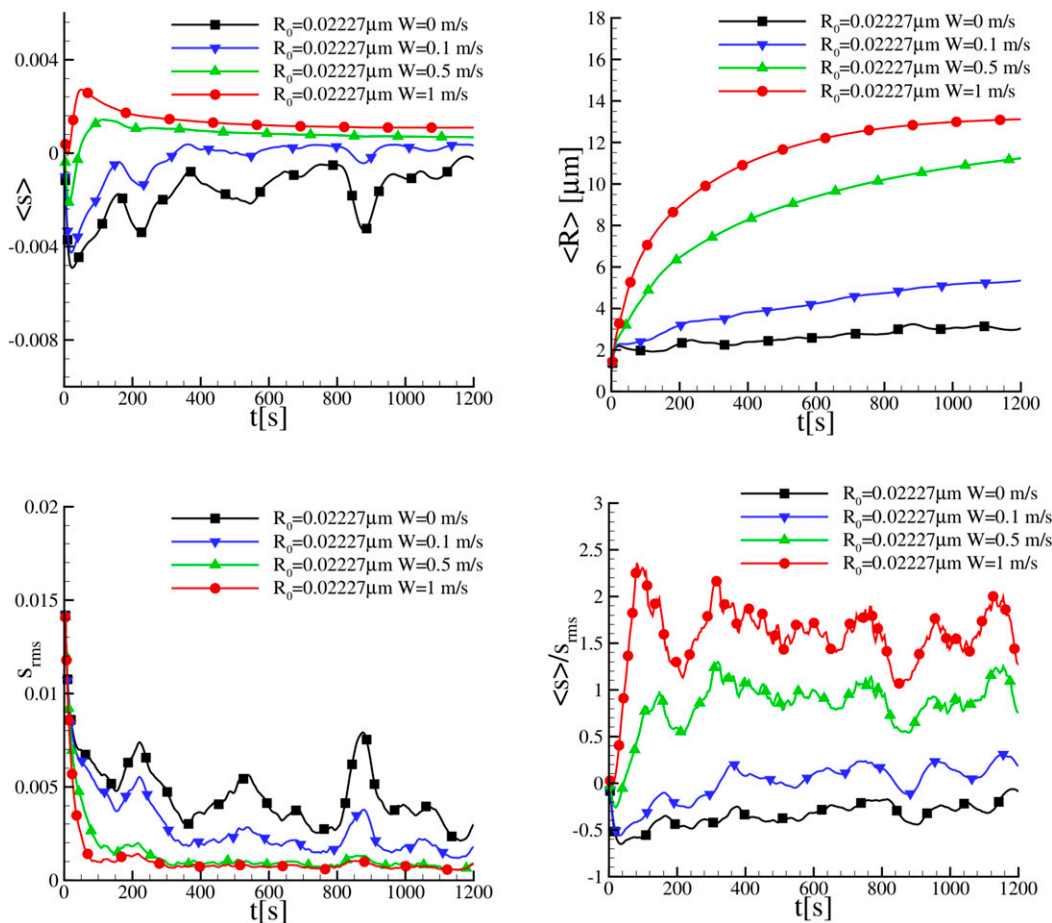
FIG. 7. Temporal evolution of (top left) mean cloud supersaturation, (top right) mean droplet radius, (bottom left) supersaturation standard deviation, and (bottom right) ratio between mean and standard deviation supersaturation for NaCl salt CCN.

5. Discussion and conclusions

A series of LESs of homogeneous isotropic turbulence has been analyzed to illustrate the growth of water droplets via condensation/evaporation in turbulent clouds. The effects of a mean-flow vertical updraft and of the droplet nucleus chemical compositions have been also investigated. In particular, in absence of updraft the droplet squared radii follow a classical random walk behavior, as already described in our previous work (Sardina et al. 2015). The standard deviation of the droplet size distribution increases in time as a power law, $t^{1/2}$. At fixed time, the standard deviation of the droplet size distribution is bounded by the value of the quasi-equilibrium supersaturation s^{qs} (Grabowski and Wang 2013) and is proportional to the larger turbulent scales of the cloud $L^{2/3}$. This scenario is modified by the presence of a mean updraft velocity: the power law exponent becomes less than 1/2, and the standard deviation is observed to asymptote to a constant for updraft

velocities on the order of $1\,m\,s^{-1}$. The overall effect is a reduction of the droplet growth, in agreement with the results from the simulations of Gotoh et al. (2016). We have presented an extended stochastic model that, for the first time, is able to analytically predict this reduction in droplet spectral broadening. The model shows that the steady-state value of the droplet distribution standard deviation is inversely proportional to the square root of the average supersaturation field and directly proportional to the turbulence Reynolds number. This result arises from the fact that a positive average supersaturation field induces a decorrelation of the radius growth from the local resolved supersaturation field.

The power-law behavior observed at zero updraft for large droplets $t^{1/2}$ is modified also in presence of small droplets on the order of the critical radius inside the cloud domain. When droplets reach the critical radius, their evaporation is blocked by the chemical properties of its salt nucleus and a deviation from a classic random
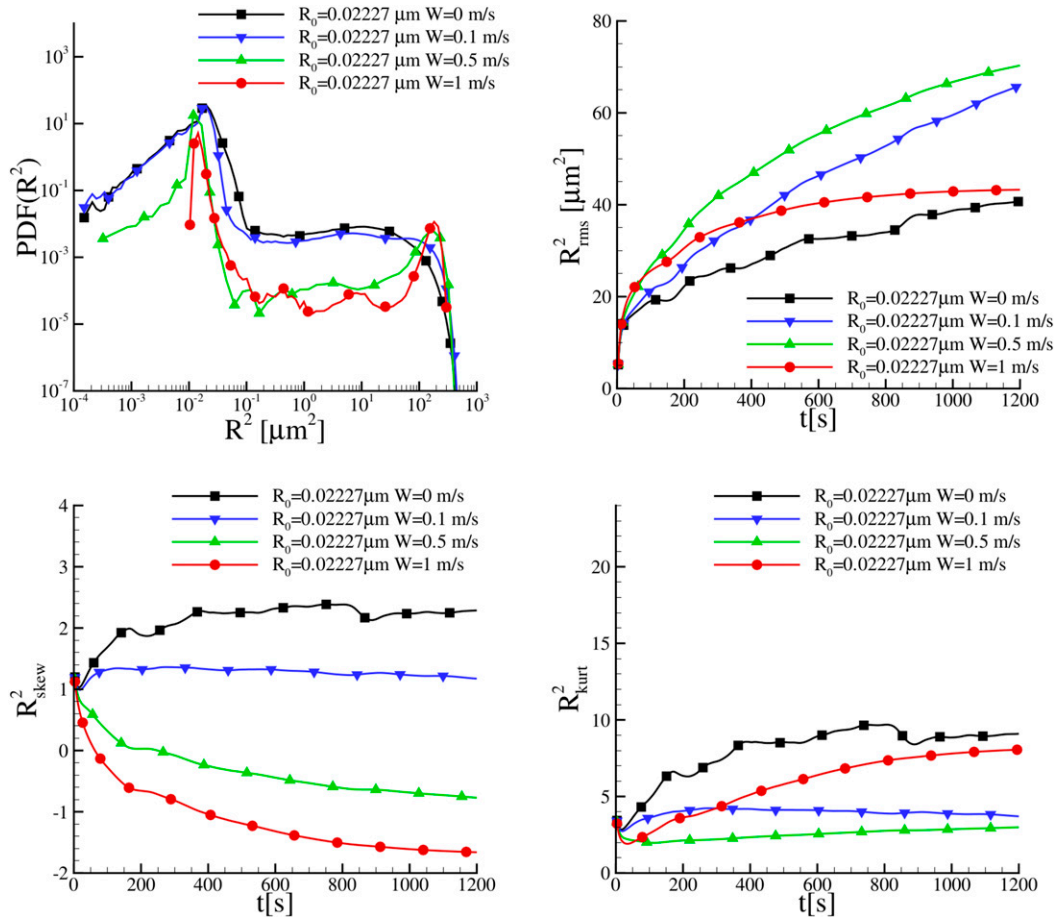
FIG. 8. (top left) Squared droplet radii probability density function pdf after 20 min of simulation for NaCl salt CCN. Temporal evolution of square droplet radius (top right) standard deviation, (bottom left) skewness, and (bottom right) kurtosis for NaCl salt CCN.

walk behavior is observed. This is associated to the saturation of the droplet growth for the zero-updraft case and reflected in the droplet squared-radius spectra. While for large particles the distribution is purely Gaussian, smaller particles tend to strongly deviate from a Gaussian behavior. The right tail of the distribution tends to resemble a Gaussian behavior while the left tail is characterized by a peak in correspondence of the haze activation radius. The strong deviations of the droplet spectrum from a Gaussian distribution will be crucial for the later stages of droplet growth, which are dominated by droplet collisions. Growth by turbulent and gravitationally induced collisions strongly depends on both droplet size and droplet number distributions. For the NaCl CCN we observe the existence of six orders of magnitude difference between the squared radii of the larger and smaller droplets, associated with a similar difference in droplet terminal velocity. This huge difference in droplet terminal velocity can enhance the

efficiency of gravitational collisions. The study of turbulence induced collisions is fundamental to continue the investigation of the size gap in warm-cloud rain formation. Droplet collisions occur at small scales so that an LES technique is not suitable to investigate this phenomenology. Novel highly resolved DNSs are needed to address this phenomenology and to be able to derive new collision kernel and models to be incorporated in an LES. The simulations described in the paper represent a unique dataset to study the effect of CCN activation/deactivation in three-dimensional homogeneous isotropic turbulence and can be used to improve the current microphysical models in the presence of turbulence.

REFERENCES

Bartlett, J., and P. Jonas, 1972: On the dispersion of the sizes of droplets growing by condensation in turbulent clouds. *Quart. J. Roy. Meteor. Soc.*, **98**, 150–164, https://doi.org/10.1002/qj.49709841512.

Beals, M. J., J. P. Fugal, R. A. Shaw, J. Lu, S. M. Spuler, and J. L. Stith, 2015: Holographic measurements of inhomogeneous cloud mixing at the centimeter scale. *Science*, **350**, 87–90, https://doi.org/10.1126/science.aab0751.

Bewley, J. L., and S. Lasher-Trapp, 2011: Progress on predicting the breadth of droplet size distributions observed in small cumuli. *J. Atmos. Sci.*, **68**, 2921–2929, https://doi.org/10.1175/JAS-D-11-0153.1.

Brenguier, J.-L., and L. Chaumat, 2001: Droplet spectra broadening in cumulus clouds. Part I: Broadening in adiabatic cores. *J. Atmos. Sci.*, **58**, 628–641, https://doi.org/10.1175/1520-0469(2001)058<0628:DSBICC>2.0.CO;2.

Celani, A., A. Mazzino, A. Seminara, and M. Tizzi, 2007: Droplet condensation in two-dimensional Bolgiano turbulence. *J. Turbul.*, **8**, N17, https://doi.org/10.1080/14685240601105716.

——, ——, and M. Tizzi, 2008: The equivalent size of cloud condensation nuclei. *New J. Phys.*, **10**, 075021, https://doi.org/10.1088/1367-2630/10/7/075021.

——, ——, and ——, 2009: Droplet feedback on vapor in a warm cloud. *Int. J. Mod. Phys.*, **23B**, 5434–5443, https://doi.org/10.1142/S0217979209063754.

Chandrakar, K. K., W. Cantrell, K. Chang, D. Ciochetto, D. Niedermeier, M. Ovchinnikov, R. A. Shaw, and F. Yang, 2016: Aerosol indirect effect from turbulence-induced broadening of cloud-droplet size distributions. *Proc. Natl. Acad. Sci. USA*, **113**, 14 243–14 248, https://doi.org/10.1073/pnas.1612686113.

Cooper, W. A., 1989: Effects of variable droplet growth histories on droplet size distributions. Part I: Theory. *J. Atmos. Sci.*, **46**, 1301–1311, https://doi.org/10.1175/1520-0469(1989)046<1301:EOVDGH>2.0.CO;2.

——, S. G. Lasher-Trapp, and A. M. Blyth, 2011: Initiation of coalescence in a cumulus cloud: A beneficial influence of entrainment and mixing. *Atmos. Chem. Phys. Discuss.*, **11**, 10 557–10 613, https://doi.org/10.5194/acpd-11-10557-2011.

de Lozar, A., and L. Muessle, 2016: Long-resident droplets at the stratocumulus top. *Atmos. Chem. Phys.*, **16**, 6563–6576, https://doi.org/10.5194/acp-16-6563-2016.

Devenish, B., and Coauthors, 2012: Droplet growth in warm turbulent clouds. *Quart. J. Roy. Meteor. Soc.*, **138**, 1401–1429, https://doi.org/10.1002/qj.1897.

Falkovich, G., A. Fouxon, and M. Stepanov, 2002: Acceleration of rain initiation by cloud turbulence. *Nature*, **419**, 151–154, https://doi.org/10.1038/nature00983.

Gotoh, T., T. Suehiro, and I. Saito, 2016: Continuous growth of cloud droplets in cumulus cloud. *New J. Phys.*, **18**, 043042, https://doi.org/10.1088/1367-2630/18/4/043042.

Grabowski, W. W., and L.-P. Wang, 2013: Growth of cloud droplets in a turbulent environment. *Annu. Rev. Fluid Mech.*, **45**, 293–324, https://doi.org/10.1146/annurev-fluid-011212-140750.

——, and G. C. Abade, 2017: Broadening of cloud droplet spectra through eddy hopping: Turbulent adiabatic parcel simulations. *J. Atmos. Sci.*, **74**, 1485–1493, https://doi.org/10.1175/JAS-D-17-0043.1.

Jensen, J. B., and A. D. Nugent, 2017: Condensational growth of drops formed on giant sea-salt aerosol particles. *J. Atmos. Sci.*, **74**, 679–697, https://doi.org/10.1175/JAS-D-15-0370.1.

Köhler, H., 1936: The nucleus in and the growth of hygroscopic droplets. *Trans. Faraday Soc.*, **32**, 1152–1161, https://doi.org/10.1039/TF9363201152.

Kostinski, A., 2009: Simple approximations for condensational growth. *Environ. Res. Lett.*, **4**, 015005, https://doi.org/10.1088/1748-9326/4/1/015005.

Kumar, B., J. Schumacher, and R. A. Shaw, 2014: Lagrangian mixing dynamics at the cloudy–clear air interface. *J. Atmos. Sci.*, **71**, 2564–2580, https://doi.org/10.1175/JAS-D-13-0294.1.

Lanotte, A. S., A. Seminara, and F. Toschi, 2009: Cloud droplet growth by condensation in homogeneous isotropic turbulence. *J. Atmos. Sci.*, **66**, 1685–1697, https://doi.org/10.1175/2008JAS2864.1.

Lasher-Trapp, S. G., W. A. Cooper, and A. M. Blyth, 2005: Broadening of droplet size distributions from entrainment and mixing in a cumulus cloud. *Quart. J. Roy. Meteor. Soc.*, **131**, 195–220, https://doi.org/10.1256/qj.03.199.

Lau, K. M., and H. T. Wu, 2003: Warm rain processes over tropical oceans and climate implications. *Geophys. Res. Lett.*, **30**, 2290, https://doi.org/10.1029/2003GL018567.

Levin, L., and Y. S. Sedunov, 1966: Stochastic condensation of drops and kinetics of cloud spectrum formation. *J. Rech. Atmos.*, **2**, 425–432.

Li, X.-Y., A. Brandenburg, N. Haugen, and G. Svensson, 2017: Eulerian and Lagrangian approaches to multidimensional condensation and collection. *J. Adv. Model. Earth Syst.*, **9**, 1116–1137, doi:10.1002/2017MS000930.

Magaritz-Ronen, L., M. Pinsky, and A. Khain, 2014: Effects of turbulent mixing on the structure and macroscopic properties of stratocumulus clouds demonstrated by a Lagrangian trajectory model. *J. Atmos. Sci.*, **71**, 1843–1862, https://doi.org/10.1175/JAS-D-12-0339.1.

Mazin, I., 1968: Stochastic condensation and its effect on formation of cloud drop-size distribution. *Bull. Amer. Meteor. Soc.*, **49**, 595.

Mazzitelli, I. M., F. Fornarelli, A. S. Lanotte, and P. Oresta, 2014a: Pair and multi-particle dispersion in numerical simulations of convective boundary layer turbulence. *Phys. Fluids*, **26**, 055110, https://doi.org/10.1063/1.4878318.

——, F. Toschi, and A. S. Lanotte, 2014b: An accurate and efficient Lagrangian sub-grid model. *Phys. Fluids*, **26**, 095101, https://doi.org/10.1063/1.4894149.

Olivieri, S., F. Picano, G. Sardina, D. Iudicone, and L. Brandt, 2014: The effect of the Basset history force on particle clustering in homogeneous and isotropic turbulence. *Phys. Fluids*, **26**, 041704, https://doi.org/10.1063/1.4871480.

Paoli, R., and K. Shariff, 2009: Turbulent condensation of droplets: Direct simulation and a stochastic model. *J. Atmos. Sci.*, **66**, 723–740, https://doi.org/10.1175/2008JAS2734.1.

Pope, S. B., 2000: *Turbulent Flows.* Cambridge University Press, 802 pp.

Pruppacher, H., and J. Klett, 1997: *Microphysics of Clouds and Precipitation.* Springer, 954 pp.

Riechelmann, T., U. Wacker, K. D. Beheng, D. Etling, and S. Raasch, 2015: Influence of turbulence on the drop growth in warm clouds, Part II: Sensitivity studies with a spectral bin microphysics and a Lagrangian cloud model. *Meteor. Z.*, **24**, 293–311, https://doi.org/10.1127/metz/2015/0608.

Rogallo, R., 1981: Numerical experiments in homogeneous turbulence. NASA Tech. Memo. 81315, 91 pp., https://ntrs.nasa.gov/archive/nasa/casi.ntrs.nasa.gov/19810022965.pdf.

Sardina, G., F. Picano, L. Brandt, and R. Caballero, 2015: Continuous growth of droplet size variance due to condensation in turbulent clouds. *Phys. Rev. Lett.*, **115**, 184501, https://doi.org/10.1103/PhysRevLett.115.184501.

Shima, S., K. Kusano, A. Kawano, T. Sugiyama, and S. Kawahara, 2009: The super-droplet method for the numerical simulation of clouds and precipitation: A particle-based and probabilistic microphysics model coupled with a non-hydrostatic model. *Quart. J. Roy. Meteor. Soc.*, **135**, 1307–1320, https://doi.org/10.1002/qj.441.

Siebert, H., and R. A. Shaw, 2017: Supersaturation fluctuations during the early stage of cumulus formation. *J. Atmos. Sci.*, **74**, 975–988, https://doi.org/10.1175/JAS-D-16-0115.1.

Siewert, C., J. Bec, and G. Krstulovic, 2017: Statistical steady state in turbulent droplet condensation. *J. Fluid Mech.*, **810**, 254–280, https://doi.org/10.1017/jfm.2016.712.

Smagorinsky, J., 1963: General circulation experiments with the primitive equations: I. The basic experiment. *Mon. Wea. Rev.*, **91**, 99–164, https://doi.org/10.1175/1520-0493(1963)091<0099:GCEWTP>2.3.CO;2.

Srivastava, R., 1989: Growth of cloud drops by condensation: A criticism of currently accepted theory and a new approach. *J. Atmos. Sci.*, **46**, 869–887, https://doi.org/10.1175/1520-0469(1989)046<0869:GOCDBC>2.0.CO;2.

Sundaram, S., and L. R. Collins, 1997: Collision statistics in an isotropic particle-laden turbulent suspension. Part 1. Direct numerical simulations. *J. Fluid Mech.*, **335**, 75–109, https://doi.org/10.1017/S0022112096004454.

Twomey, S., 1959: The nuclei of natural cloud formation part II: The supersaturation in natural clouds and the variation of cloud droplet concentration. *Pure Appl. Geophys.*, **43**, 243–249, https://doi.org/10.1007/BF01993560.

Vaillancourt, P. A., and M. K. Yau, 2000: Review of particle–turbulence interactions and consequences for cloud physics. *Bull. Amer. Meteor. Soc.*, **81**, 285–298, https://doi.org/10.1175/1520-0477(2000)081<0285:ROPIAC>2.3.CO;2.

——, ——, P. Bartello, and W. W. Grabowski, 2002: Microscopic approach to cloud droplet growth by condensation. Part II: Turbulence, clustering, and condensational growth. *J. Atmos. Sci.*, **59**, 3421–3435, https://doi.org/10.1175/1520-0469(2002)059<3421:MATCDG>2.0.CO;2.

Warner, J., 1969: The microstructure of cumulus cloud. Part I. General features of the droplet spectrum. *J. Atmos. Sci.*, **26**, 1049–1059, https://doi.org/10.1175/1520-0469(1969)026<1049:TMOCCP>2.0.CO;2.